



**HAL**  
open science

## Observing the subglacial hydrology network and its dynamics with a dense seismic array

Ugo Nanni, Florent Gimbert, Philippe Roux, Albanne Lecointre

► **To cite this version:**

Ugo Nanni, Florent Gimbert, Philippe Roux, Albanne Lecointre. Observing the subglacial hydrology network and its dynamics with a dense seismic array. Proceedings of the National Academy of Sciences of the United States of America, 2021, 118, 10.1073/pnas.2023757118 . insu-03594399

**HAL Id: insu-03594399**

**<https://insu.hal.science/insu-03594399>**

Submitted on 5 Apr 2024

**HAL** is a multi-disciplinary open access archive for the deposit and dissemination of scientific research documents, whether they are published or not. The documents may come from teaching and research institutions in France or abroad, or from public or private research centers.

L'archive ouverte pluridisciplinaire **HAL**, est destinée au dépôt et à la diffusion de documents scientifiques de niveau recherche, publiés ou non, émanant des établissements d'enseignement et de recherche français ou étrangers, des laboratoires publics ou privés.



1

2 **Main Manuscript for**

3 Observing the subglacial hydrology network and its dynamics with a  
4 dense seismic array

5 Ugo Nanni<sup>1</sup>, Florent Gimbert<sup>1</sup>, Philippe Roux<sup>2</sup> and Albanne Lecointre<sup>2</sup>

6 <sup>1</sup>, IGE, Univ. Grenoble Alpes, CNRS, IRD, Grenoble, France

7 <sup>2</sup>, ISTerre, Univ. Grenoble Alpes, Univ. Savoie Mont Blanc, CNRS, IRD, IFSTTAR, Grenoble,  
8 France

9 \* Ugo Nanni

10 **Email:** [ugo.nanni@univ-grenoble-alpes.fr](mailto:ugo.nanni@univ-grenoble-alpes.fr)

11 **Author Contributions:**

12 U.N., F.G., P.R. designed the study; U.N., F.G., P.R. participated in the field installations; U.N.,  
13 F.G., P.R., A.L. performed the research; U.N., F.G., P.R., A.L. analyzed the data; U.N. wrote the  
14 paper with help from F.G. and P.R.

15 **Competing Interest Statement:**

16 The authors declare that they have no competing financial interests

17 **Classification:**

18 Physical Sciences - Earth, Atmospheric, and Planetary Sciences

19 **Keywords:**

20 Cryoseismology – Subglacial hydrology – dense seismic array – seismic noise sources

21 **This PDF file includes:**

22 Main Text

23 Figures 1 to 4

24 **Abstract**

25 Subglacial water flow strongly modulates glacier basal motion, which itself strongly influences the  
26 contributions of glaciers and ice sheets to sea-level rise. However, our understanding of when and  
27 where subglacial water flow enhances or impedes glacier flow is limited due to the paucity of direct  
28 observations of subglacial drainage characteristics. Here we demonstrate that dense seismic array  
29 observations combined with an innovative systematic seismic source location technique allows for  
30 the first time the retrieval of a two-dimensional map of a subglacial drainage system, as well as its  
31 day-to-day temporal evolution. We observe with unprecedented detail when and where subglacial  
32 water flows through a cavity-like system that enhances glacier flow versus when and where water  
33 mainly flows through a channel-like system that impedes glacier flow. Most importantly, we are  
34 able to identify regions of high hydraulic connectivity within and across the cavity and channel  
35 systems, which have been identified as having a major impact on the long term glacier response  
36 to climate warming. Applying a similar seismic monitoring strategy in other glacier settings,  
37 including for ice sheets, may help to diagnose the susceptibility of their dynamics to increased  
38 meltwater input due to climate warming.

39 **Significance Statement**

40 Our understanding of when, where and under which conditions subglacial water flow favors or  
41 impedes glacier flow remains uncertain mainly because of sparse field observations. This strongly  
42 limits our capability to assess the susceptibility of glaciers and ice-sheets to a future increase in  
43 meltwater input due to climate warming. Here we overcome classic observational difficulties by  
44 establishing an innovative seismic-based approach. From dense-seismic array observations we  
45 retrieve with unprecedented detail the two-dimensional map of a subglacial hydrology network.  
46 We observe its day-to-day evolution from a cavity-dominated system that favors glacier flow to a  
47 channel-dominated system that impedes glacier flow. Although our method was applied on an  
48 Alpine Glacier, it is easily adaptable and readily applicable to other settings such as Greenland or  
49 Antarctica.

50

51 **Main Text**

52

53 **Introduction**

54

55 Meltwater produced at the surface of a glacier is mostly routed to its bed through crevasses and  
56 moulins and flows towards its terminus through the subglacial drainage system<sup>1</sup>. In this system,  
57 water pressure regulates the ice–bed mechanical coupling, which determines the glacier sliding  
58 speed, and therefore has major effects on the stability of glaciers and ice sheets<sup>2,3</sup> and their  
59 contributions to sea-level rise<sup>4–6</sup>. Subglacial water pressure shows complex dependency on the  
60 subglacial route that the water follows, and in particular on whether the water flows through a  
61 distributed and inefficient system<sup>7</sup> (e.g. cavity-dominated for hard bed glaciers) or a localized and  
62 efficient system<sup>8</sup> (channel-dominated drainage system is expected to be associated with a,  
63 comparatively, lower water pressure, which promotes low glacier sliding speeds<sup>8,10–12</sup>. Where  
64 cavities are hydraulically well connected to channels they drain into the efficient drainage  
65 system, which tends to lower the overall water pressure<sup>13</sup>. In addition, recent observations<sup>13</sup>

66 suggested that hydraulically isolated areas of the bed with very low permeability<sup>15</sup> regulate glacier  
67 basal traction during winter<sup>16</sup> and over multi-annual timescales<sup>17</sup>. The spatial persistence of high  
68 water pressure at the glacier bed<sup>14</sup> thus depends on the subglacial drainage system configuration  
69 and the hydraulic connectivity across the cavities and from the cavities to the channels. However,  
70 current observations of subglacial drainage systems are rather point-scale<sup>14,18</sup> (e.g., via ice-  
71 drilling) or spatially-integrated<sup>19,20</sup> (e.g. via dye tracing experiments or hydrochemical analysis),  
72 such that they provide only partial representations of the heterogeneous nature of the subglacial  
73 drainage system. It thus remains uncertain where and when isolated cavities, connected cavities,  
74 and/or channels operate, and therefore under what conditions (e.g., water supply rate, glacier  
75 geometry) meltwater supply to the glacial bed enhances or limits glacier flow.

76 Recent studies have indicated that turbulent subglacial water flow generates detectable seismic  
77 noise<sup>21</sup> given flow velocities of the order of a meter per second<sup>22</sup>, that can be used to retrieve the  
78 physical properties of subglacial channels (e.g., water pressure, conduit size)<sup>22,23</sup> as well as to  
79 estimate their location in space<sup>24,25</sup>. Previous studies that have attempted to spatially track water  
80 flow have documented their azimuthal distribution, but not their epicentral coordinates<sup>24–26</sup>.

81 Location of epicentral coordinates of simultaneously active and spatially spread noise sources  
82 indeed represents a major seismological challenge<sup>27</sup>, since it requires observations of the  
83 wavefield all around the targeted sources with high enough resolution to deal with its strong  
84 incoherency<sup>28,29</sup>. Here, we demonstrate that well-resolved maps of subglacial drainage systems  
85 can be retrieved using particularly dense seismic arrays and by adapting the matched-field  
86 processing (MFP) technique<sup>28</sup> to the particularity of dealing with spatially spread sources.

### 87 **Seismic monitoring and source location strategy**

88 We use the 1-month seismic record from 98 three-component sensors that was acquired at the  
89 surface of glacier d'Argentière (French Alps; Fig. 1) during the onset of the 2018 melt-season  
90 (see Methods and ref.<sup>30</sup> for detailed description of the experiment and ref.<sup>23</sup> for a broader  
91 glaciological context). At this location, subglacial water flow strongly influences glacier dynamics<sup>31</sup>

92 and generates continuous seismic noise that is most pronounced in the [3-7] Hz frequency  
93 range<sup>23</sup>, in which seismic wavelengths are on the order of [200-500] m<sup>32</sup>. Our seismic array  
94 covers an area of 400 x 600 m<sup>2</sup> with a 40-m to 50-m sensor spacing and an aperture (i.e. largest  
95 distance between stations; Fig. 1) of ca. 720m. Such configuration allows subwavelength  
96 sampling while covering all azimuthal directions around the targeted sources, which are two  
97 necessary conditions for retrieving the epicentral coordinates of seismic sources through  
98 application of MFP<sup>28,29</sup>(Methods). MFP consists of recursively matching the predicted and  
99 observed phase delays (Methods), and has been extensively applied to locate spatially well-  
100 separated sources, such as those generated by hydrothermal activity<sup>33</sup>, oil and gas injection<sup>34</sup>,  
101 icequakes<sup>32</sup>, or englacial moulines<sup>32</sup>. However, it has been little applied to locate spatially  
102 distributed noise sources<sup>34,35</sup>. We adapt this technique to provide such particularity through a  
103 systematic analysis of the phase coherence over 1-s-long time windows. Within each window, we  
104 apply an efficient gradient-based minimization algorithm that allows us to locate up to 29  
105 simultaneously active sources (Methods). We obtain each source location from maximizing the  
106 correlation between the observed and the modeled phase delays. We refer to this maximum  
107 correlation as the MFP output, which ranges from 0 to 1. An MFP output close to 1 indicates  
108 global phase coherence, as expected for a dominant and punctual source<sup>36</sup>, while a low MFP  
109 output indicates several local phase coherences, as expected for multiple sources simultaneously  
110 acting over the area. We note that we only keep the sources that are located within 400 m of the  
111 center of our array and are associated with realistic physical properties (i.e., wave velocities,  
112 source depth; Fig. 2b, c). This yields more than a million seismic sources per day (Fig. 2a).

### 113 **Retrieving the geometry of the subglacial system**

114 In Figure 2d, e, we show the normalized spatial distribution probability of the source location  
115 obtained over the study period for high and low MFP output ranges, as indicated in Figure 2a. We  
116 observe that events associated with high (i.e., global) phase coherence (MFP output, >0.8) are  
117 mainly located at the glacier surface (Fig. 2b) where crevasses are observed (Fig. 2e), and are

118 associated with phase velocities that are typical of surface waves<sup>37</sup> (ca. 1580 m.s<sup>-1</sup>; Fig. 2c). This  
119 is consistent with these events corresponding to crevasse-induced icequakes (Fig. 1). On the  
120 contrary, sources associated with low (i.e., local) phase coherence (MFP output, [0.05-0.3]) are  
121 preferentially located at depth near the ice–bed interface (Fig. 2b). The associated phase  
122 velocities (Fig. 2c) vary by up to ca. 3600 m.s<sup>-1</sup>, which is consistent with body waves being  
123 generated additionally to surface waves, and thus with sources that occur at depth<sup>38</sup>. The spatial  
124 distribution of these sources show two elongated regions located along the glacier centerline (one  
125 at maximum ice thickness and one 50 m further down-glacier) where hydraulic potential  
126 calculations allow materializing the likely location of subglacial channel(s) (Fig. 2d; see Methods  
127 for details on the hydraulic potential calculations). All of these concomitant features lead us to  
128 interpret these observed seismic sources as a depiction of the geometry of the subglacial  
129 drainage system. The characteristic width of the observed spots (ca. 50 m, Fig. 2d) is much  
130 greater than might be expected for a single subglacial channel (on the order of meter to few  
131 meters<sup>8</sup>), which could result from the location resolution being limited by the seismic wavelength  
132 investigated (expected to be 1/6 to 1/2 times the ca. 300m wavelength; see Methods) or from the  
133 presence of multiple channels. The absence of clear source locations in the up-glacier part of the  
134 array (Fig. 3) might be caused by reduced or less turbulent subglacial water flow there, compared  
135 to the down-glacier part, where over-deepening of the glacier bed might favor unstable and more  
136 turbulent water flow<sup>39</sup>.

137

### 138 **Observing the switch from a cavity-like to a channel-like drainage system**

139 We further investigate whether with our observational technique we can retrieve the different  
140 components of a subglacial drainage system by evaluating temporal changes in the source  
141 location maps together with the subglacial flow parameters that characterize average water  
142 drainage efficiency and water pressure conditions at the glacier bed<sup>22,23</sup> (see Methods for details).  
143 We calculate source location maps averaged over 2-day time windows (Fig. 3) and use the

144 combined seismic signal amplitude and water discharge measurements to invert for spatially-  
145 integrated changes in the hydraulic pressure gradient and hydraulic radius of the subglacial  
146 drainage system (Fig. 4)<sup>22,23</sup>. All maps are obtained from sources yielding a similar phase  
147 coherence (i.e. associated with MFP output within the same narrow [0.07-0.16] range) such that  
148 they are retrieved with a similar accuracy (see Methods).

149 We observe that sources are spatially more distributed at the beginning of the period (until ca.  
150 May 10; Fig. 3) than when averaging source locations over the whole period (Fig. 2d). At this time  
151 the hydraulic pressure gradient (Fig. 4a, green line) varies significantly with the discharge (from  
152  $0.1 \text{ m}^3 \cdot \text{s}^{-1}$  to  $2 \text{ m}^3 \cdot \text{s}^{-1}$ ; Fig. 4b, blue line) and the hydraulic radius remains constant (Fig. 4a, purple  
153 line), which indicates low drainage efficiency<sup>23</sup>. This time period is also associated with marked  
154 glacier surface acceleration (velocity increases by up to ca. 50%) due to enhanced basal sliding<sup>31</sup>  
155 as a result of the subglacial water pressurization<sup>7</sup>. These concomitant observations provide  
156 strong support that with our source location analysis we can observe water flow in the cavity-like  
157 system. This has not been suggested in previous cryoseismic studies<sup>21-23,25</sup> on the premise that  
158 fast and turbulent water flow speeds (as  $\text{m} \cdot \text{s}^{-1}$ ; i.e., seismically detectable<sup>22</sup>) only occur in  
159 channels. However this is consistent with borehole field observations<sup>14,40</sup> and with theoretical  
160 studies that have envisioned channel-like flow in connections between cavities (referred to as  
161 orifices)<sup>9</sup>.

162 While progressing through time (from ca. May 10), the subglacial water flow localizes into a  
163 narrower zone (Fig. 3). This transition towards a channel-dominated system is well revealed by  
164 the significant increase in the two-dimensional coefficient of determination  $R^2$  (Fig. 4a) calculated  
165 between the spatial pattern observed for May 25-26 (Fig. 3o) and each of the patterns shown in  
166 Figure 3. Concomitantly, and in contrast to the first part of the period, we observe a doubling of  
167 the hydraulic radius with a reduced and almost unvarying hydraulic pressure gradient, which  
168 indicates that the increasing drainage efficiency lowers the basal water pressure. Such an  
169 increase in drainage efficiency is consistent with the increase in water discharge not resulting in



170 glacier acceleration, but rather in slight deceleration<sup>41</sup>. Our seismic analysis therefore provides  
171 independent observational support for the hypothesis that the development of an efficient and  
172 channel-like system reduces the basal water pressure and favors slower glacier flow.

173

174 **Implications for the monitoring of hydraulic connectivity within and across subglacial**  
175 **drainage systems**

176 The presence of seismically detectable turbulent water flow within the cavity-like drainage system  
177 suggests that this system is, at least in certain places, associated with high hydraulic connectivity.

178 The absence of seismic sources over many areas of the glacier bed indicates that these,  
179 comparatively, have lower hydraulic connectivity, and could correspond to hydraulically isolated  
180 portions of the bed with higher potential for water storage<sup>13,15</sup>. This shows not only that our  
181 seismic analysis can determine when and where the transition from a cavity-like to a channel-like  
182 system occurs, but also that it can identify locations with high hydraulic connectivity within the  
183 cavity-like system and from the cavity- to the channel-like systems. This implies that we can  
184 evaluate which areas of the glacier bed are efficiently connected to channels, and thus drained  
185 when they develop, versus the areas where water is stored and is thought to regulate the basal  
186 traction over multi-year timescales<sup>15,17</sup>. Yielding such observations in other settings like  
187 Greenland has the potential for identifying locations where ice dynamics are expected to be  
188 particularly sensitive to the foreseen increase in melt water input rates due to climate warming<sup>3</sup>.

189 **Perspectives and limitations**

190 A successful application of our methodology to other glacier systems like Ice-Sheet outlet glaciers  
191 relies on the capability to conduct subwavelength sampling over representative areas (Methods),  
192 ranging from about 1x1km<sup>2</sup> (e.g. Russel Glacier's tongue<sup>42</sup>) up to about 10x10km<sup>2</sup> (e.g. central  
193 trunk of Pine Island Glacier<sup>43</sup>). These scaling constraints can be can be fulfilled through deploying  
194 c. 100 up to c. 10,000 sensors in these areas, which we foresee as achievable in the near future  
195 given the recent ease of dense seismic array installations in remote areas<sup>44-46</sup>.

196 Although the present seismic approach yields unprecedented insights on subglacial hydrology from  
197 the local (Fig. 3) up to the glacier (Fig. 4) scales, future applications will likely still strongly benefit  
198 from combination with complementary in-situ observations. Such a combination will guide the  
199 strategy for conducting local (e.g., via ice-drilling) or spatially-integrated (e.g. via dye tracing  
200 experiments or hydrochemical analysis) measurements in targeted and representative places  
201 identified from the seismic observations. Complementary measurements in those targeted places  
202 will also help enhance the level of quantitative interpretation of seismic observations through  
203 giving more quantitative constraints on the behavior of key physical variables (pressure, flow  
204 speed, connectivity) in each identified subglacial hydrology system. This integrated strategy will  
205 allow to better extrapolate physical constraints from the local up to the glacier-wide scale, which  
206 will ultimately facilitate the assimilation of seismic observations in subglacial hydrology – ice  
207 dynamics coupled models, which otherwise remain poorly constrained across scales<sup>47</sup>.

## 208 **Conclusion**

209 In this study, we provide well-resolved spatial observations of a localized efficient channel-like  
210 system geometry and of the extent of a distributed inefficient cavity-like system. We show that  
211 with an adapted systematic seismic investigation of low spatial phase coherences we can locate  
212 multiple seismic noise sources induced by subglacial water flow that act at the same time. This  
213 location procedure is feasible from very low water discharge ( $\sim 0.1 \text{ m}^3 \cdot \text{s}^{-1}$ ) to peak melt-season  
214 water discharge. Thus, we can simultaneously observe the distributed and localized drainage  
215 systems through time and space, and evaluate the hydraulic connectivity within and across these  
216 systems along with their changes through time. Our geophysical approach is also exportable to  
217 other glaciers in remote areas, from mountain glaciers to ice caps, especially with the current  
218 easing of dense-seismic arrays<sup>46</sup> and distributed acoustic sensing<sup>44,48</sup> deployments. Our novel  
219 way of investigating subglacial drainage systems will allow the glaciological community to  
220 diagnose the susceptibility of ice sheets<sup>15,17</sup> and mountain glaciers<sup>14,47</sup> to increased meltwater  
221 input due to climate warming and/or extreme melt and rainfall events. Our approach will also be

222 particularly appropriate to study processes that generate similar spatially spread seismic noise in  
223 other environments, such as for lava flows on volcanoes<sup>49</sup>, tremors in fault zones<sup>50</sup>, and sediment  
224 transport in rivers<sup>51</sup>.

225

## 226 **Materials and Methods**

227

### 228 *Dense seismic array survey*

229 All of the stations have a 500-Hz sampling rate and a low cut-off frequency of 4.5 Hz. The nodes  
230 were installed at a depth of 30 cm into the 4-m-thick snow cover, and had to be reinstalled on  
231 May 11 due to snow melt, which occurred at a rate of 5 cm.day<sup>-1</sup>. We refer the reader to ref.<sup>30</sup> for  
232 the detailed description of the experiment.

### 233 *Complementary measurements*

234 Concomitant with our seismic survey, we use continuous records of subglacial water discharge,  
235 which was measured in excavated subglacial tunnels maintained by the hydroelectric power  
236 company Emosson S.A. at ca. 600 m downstream of the center of the node-array (at 2173 m  
237 a.s.l.). We also installed four GNSS stations at the corners of the seismic array to measure glacial  
238 surface velocity, which was on the order of 0.1 m.day<sup>-1</sup> at this time of the year and for this part of  
239 the glacier<sup>31</sup>. One week prior to the seismic deployment, we conducted a ground penetrating  
240 radar campaign over the study area with a 5-MHz signal, to improve the previous estimates of the  
241 bed topography reported by ref. <sup>52</sup>. Also, in September 2018, we conducted an aerial survey to  
242 derive a digital elevation model of the glacier surface using stereo-photogrammetry. Combining  
243 these two digital elevation models, we calculated the ice thickness distribution over the study  
244 area, as shown in Figure 1. The ice thickness reached up to 270 m at the center of the seismic  
245 array, with a well-marked talweg (i.e., valley-shaped bed) aligned in the glacier flow direction, and  
246 a progressive diminution of the ice thickness down-glacier both within the area covered by our  
247 array and from the location of our array towards the glacier terminus. The reader should refer to

248 ref.<sup>30</sup> for the detailed description of the complementary data associated with this seismic  
249 experiment.

### 250 *Matched field processing*

251 Matched field processing (MFP) consists of providing a probabilistic estimate of the epicentral  
252 coordinate of dominant source<sup>28</sup> from evaluation of the phase coherence of the seismic signal  
253 over an array of sensors. The method consists of recursively matching the phase delays of a  
254 model-based synthetic wave-field (i.e., the ‘trial source’) with the phase delays observed between  
255 the sensors over the array. A condition for this method to be applicable is that spatially coherent  
256 phase information can be extracted between nearby sensors<sup>28</sup>, which requires interstation  
257 spacing of less than one-half of the investigated wavelength. We satisfy this conditions with our  
258 40 to 50 m interstation spacing for a 200 to 500m investigated wavelength.

259 We first compute the discrete Fourier transform of a given data vector  $d(t)$  recorded by the 98  
260 sensors over a frequency  $\omega$ , to obtain the complex data vector  $d(\omega)$  and to calculate the  
261 corresponding cross-spectral density matrix as

$$262 \quad K(\omega) = d(\omega)d^H(\omega),$$

263 where  $H$  is the Hermitian transpose. The cross-spectral density matrix captures the relative  
264 spatial phase difference between the sensors. We then define a set of values to be explored for  
265 trial sources. In this study, we set four degrees of freedom for the MFP processing, with a depth,  
266 range and phase velocity grid (X, Y, Z, C). An important condition for retrieving source epicentral  
267 coordinate (i.e. X, Y, Z) and not only source back azimuth is to have a source-to-array distance  
268 not greater than two to three times the array aperture (i.e. largest distance between stations)<sup>29</sup>.  
269 We satisfy this condition with a c. 750 m array aperture for a c. 270m source-to-station  
270 distances<sup>23</sup> (i.e. maximum glacier thickness<sup>53</sup>). For each element  $a$  of these four dimensions of  
271 the grid we model the Green’s function replica vector  $d(\omega, a)$  under the hypothesis of a  
272 homogenous medium as

273

$$d(\omega, a) = \exp\left(i\omega r_a/c\right),$$

274

where  $c$  is the medium velocity and  $r_a$  is the distance between each receiver and the trial source

275

position  $a$ .

276

To match the observed cross-spectral density matrix with the replica vector, we calculate the

277

Bartlett processor as

278

$$B_{Bartlett}(\omega, a) = \sum_{\omega} |d(\omega, a)^H K(\omega) d(\omega, a)|.$$

279

This operation is equivalent to cross-correlation between the observed wave-field phase and the

280

modeled one. We refer to the  $B_{Bartlett}(\omega)$  values as the MFP output. The MFP output is

281

calculated at specific frequencies, and ranges from 0 to 1. The closer to 1 the MFP output is, the

282

more the modeled phase matches the observations. Sources that generate a signal resulting in

283

similar phase coherence (i.e. MFP output value) are expected to be localized with a similar

284

accuracy<sup>28</sup>.

285

We perform source location over 1-s-long signal segments of the vertical component only. We

286

filter the signal within the [3-7] Hz frequency range that is the most sensitive to subglacial water

287

flow induced seismic noise<sup>21,23-25</sup>, and coherently apply the MFP for each 0.4 Hz within this

288

range. To maximize the efficiency of our algorithm and minimize the computational costs, we use

289

a gradient-based minimization algorithm (i.e., Nelder-Mead optimization<sup>54</sup>) to converge to the best

290

match between the trial and the observed phase delays, rather than exhaustive grid-search

291

exploration. The convergence criterion is reached when the variance of the values obtained over

292

the last five iterations of the optimization is  $< 1e^{-2}$ , with a maximum of 3000 iterations. Our 29

293

different starting points used for optimization are located 250 m below the glacier surface, and

294

they uniformly cover an area of  $800 \times 800 \text{ m}^2$  centered on the array (Fig. 2d). We set the initial

295

velocity to  $1800 \text{ m}\cdot\text{s}^{-1}$ . The 29 point locations found per signal segment (1 s) after convergence

296

are all located in the same place if clear global convergence exists (i.e., high MFP output) or at up

297 to 29 different locations if up to 29 local minima exist (i.e., low MFP output). The MFP output  
298 value can also be understood as an indicator of the number of receivers over which the signal is  
299 coherent; e.g., a value of 0.1 indicates a source that generates a signal coherent over 10% of the  
300 array. We found that this approach is comparable to using sub-arrays of variable sizes to perform  
301 the MFP over different areas of the glaciers. Further details on the methods and related physics  
302 can be found in ref. <sup>55</sup>.

### 303 *Matched field processing output statistics*

304 We narrow the MFP output selection by keeping only: (1) the location that yields realistic phase  
305 velocities ([1200-3600] m.s-1); and (2) the localizations at  $\pm 400$  m from the array center and  $\leq 400$   
306 m below the glacier surface. The number of located sources after this selection (Fig. 2a)  
307 decreases as the MFP output increases, with >5000 daily sources associated with MFP output  
308 <0.05, and <1 daily source associated with MFP output >0.75. Figure 2b, c shows the distribution  
309 of the source properties (vertical position), and Figure 2e, f shows the spatial probability of the  
310 source location over the complete study period for two MFP output bands of ([0.07-0.16] and  
311 [0.75-0.99]). These locations correspond to real and detectable seismic events, since MFP output  
312 is much higher than expected for random noise (see ref.<sup>30</sup>, [Fig. 9](#)). This two-dimensional  
313 representation is obtained by summing the total number of sources in each  $8 \times 8$  m<sup>2</sup> cell of an  
314  $800 \times 800$  m<sup>2</sup> (x, y) grid centered on our seismic array.

315 It is important to note that at low MFP output (e.g., [0.07-0.16]) only a few sensors distinguish the  
316 source. This leads to a shorter aperture of the effective seismic array, which limits depth  
317 resolution. The trend to higher probability of the source location at depth is however observed  
318 here for tens of thousands of sources. The 2-day averaging is long enough to gather sufficient  
319 statistics, while it is also short enough to correctly investigate the temporal evolution with high  
320 enough spatial accuracy (Fig. 3).

### 321 *Source location precision*

322 When compared to the crevasse field at our study location (Fig. 1), we observe that our MFP  
323 analysis yields source locations with MFP output  $>0.75$ , a precision in range down to 10 m (Fig.  
324 2) for an average wavelength  $\lambda$  of ca. 300 m at 5 Hz<sup>37</sup>. While the expected Rayleigh limit gives  
325 maximum resolution of  $\lambda/4$  (ca. 75 m at 5 Hz) in the far-field domains<sup>27</sup>, laboratory experiments<sup>56</sup>  
326 suggest that the seismic signal bears information of spatial structures down to  $\lambda/8$  (ca. 32 m at 5  
327 Hz) in the near-field of sources. Our unique instrumental set-up combined with our systematic  
328 analysis of phase coherence allow us to overcome the Rayleigh far-field limitations and obtain  
329 two-dimensional maps of source locations with resolution in the range of ca. 10 m for high MFP  
330 outputs. For lower MFP outputs, we expect lower resolution due to the smaller aperture of the  
331 array that is sensitive to local phase coherence. We acknowledge that the width of the area  
332 shown in Figure 2d might not represent the true width of a single subglacial channel, which is  
333 expected to be of the order of one to few meters at this location<sup>23</sup>. The observed width of c. 50 m  
334 could be due to the uncertainty for the source location or to the presence of multiple channels

### 335 *Hydraulic potential calculation*

336 We calculate the hydraulic potential  $\Phi$  following ref.<sup>1</sup>, as:

$$337 \quad \Phi = \rho_w g z_b + K[\rho_i g(z_s - z_b)],$$

338 where  $g$  is the acceleration due to gravity ( $9.81 \text{ m.s}^{-2}$ ),  $\rho_w$  is the density of water ( $1000 \text{ kg.m}^{-3}$ ),  $\rho_i$   
339 is the density of ice ( $917 \text{ kg.m}^{-3}$ ),  $z_b$  and  $z_s$  are the elevation of the glacier bed and surface (m),  
340 respectively, and  $K$  is the ratio of water pressure to ice overburden pressure; i.e., a uniform  
341 flotation fraction. A value of  $K$  near 0 represents a condition where basal water pressure is  
342 negligible in comparison to ice overburden pressure, and a value near 1 represents a condition  
343 where basal water pressure is high enough to significantly counterbalance ice overburden  
344 pressure. Here we use a flotation fraction of 0.5, which is likely to represent a case where the  
345 subglacial drainage system has developed enough to efficiently drain the bed<sup>1,57</sup>, and therefore  
346 reduce subglacial basal water pressure. We consider this flotation fraction to best represent the

347 subglacial water pressure condition in our location at the end of our study period when we  
348 observe a decreasing glacier velocity while water discharge still increases (Fig. 4a). We then  
349 calculate the water flow directions based on the hydraulic potential gradients, by following the  
350 path that minimizes the gradient with a minimum upstream area of 150 m<sup>2</sup> for the waterway, to  
351 initiate the use of TopoToolBox, developed by ref.<sup>58</sup>. We show in Figure Supp. 1 that different  
352 values of flotation fraction ( $K = [0.1, 0.5, 0.9]$ ) result in a similar predicted waterway pattern. The  
353 expected localization of subglacial water flow thus does not depend much on the flotation fraction,  
354 likely as a result of the V-shape of the Argentière glacier being particularly pronounced.

355

#### 356 *Inverting hydraulic properties using water discharge and seismic power measurements*

357 We use the theoretical framework of ref. <sup>22</sup> to invert for the hydraulic properties of subglacial  
358 turbulent water flow using simultaneous measurements of subglacial water discharge and seismic  
359 power. The seismic power  $P$  is calculated at each sensor using the vertical component of ground  
360 motion within [3-7] Hz and the Welch method over 4-s time windows with 50% overlap, as  
361 reported in ref. <sup>23</sup>. The physical framework relates the changes in the measured seismic power  $P$   
362 and discharge  $Q$  to changes in channel hydraulic radius  $R$  and hydraulic pressure gradient  $S$ . The  
363 basis of these relations is that turbulence within water flow generates frictional forces that act on  
364 the boundaries of the channels (i.e., ice, glacier bed) and create ground motion. This approach  
365 has been recently shown to be applicable over our study area<sup>23</sup>. The hydraulic radius  $R$  is defined  
366 as the ratio of the cross-sectional area of the channel flow to its wetted perimeter. The hydraulic  
367 pressure gradient  $S$  is a function of both the rate of change of water pressure and the bed slope  
368 in the flow direction. In the case of constant bed slope and channel geometry, increasing  $S$   
369 means closed and pressurizing channel flow. Both variables are defined for subglacial conduits  
370 where turbulent water flow dominates. We calculate median values of  $R$  and  $S$  using the median  
371 seismic power  $P$  over the 98 sensors and the water discharge  $Q$ , as follows



372 
$$S = S_{ref} \left( \frac{P}{P_{ref}} \right)^{24/41} \left( \frac{Q}{Q_{ef}} \right)^{-30/41},$$

373

374 
$$R = R_{ref} \left( \frac{P}{P_{ref}} \right)^{-9/82} \left( \frac{Q}{Q_{ef}} \right)^{-33/82}$$

375 where the subset ref is the reference state, which is April 26 in this study. In the main text, when  
376 referring to the temporal evolution of R and S, we therefore refer to their relative changes with  
377 respect to this reference period. We evaluate P over the [3-7] Hz frequency band, as it has been  
378 shown by ref. <sup>23</sup> to be the best suited in area for studying turbulent water flow. The reader is  
379 referred to refs. <sup>22,23</sup> for more details.

380 We stress that the inversions of hydraulic properties depend on the average seismic amplitude,  
381 with very little dependency on the spatial variations. Therefore, our inversions are to be  
382 considered independent of the source location, even if they both arise from the seismic signals.  
383 This also implies that our inversions represent averaged hydraulic conditions of the drainage  
384 system.

385 *State of knowledge on the main features of channels and cavities*

386 Cavities form in the downstream lee of bedrock bumps, due to ice sliding over the bed, and they  
387 close through ice creep. Cavities can be filled with water, which reduces the apparent rugosity of  
388 the glacier bed and weakens the ice–bed mechanical coupling<sup>39</sup>. For soft-bed glaciers, inefficient  
389 drainage systems also include unconsolidated layers of low permeability<sup>59</sup>. Weakly connected  
390 cavities can have permeability that are lower by ca. 9 orders of magnitude than that of connected  
391 cavities<sup>15</sup>. For a similar hydraulic gradient to that of connected cavities, turbulent water flow within  
392 a weakly connected system therefore requires much higher flow velocities.

393 Subglacial channels can be of the R-type<sup>8</sup> when melted into the ice by turbulent dissipation of  
394 heat, or of the N-type<sup>60</sup> when dug into the basal sediments by the flowing water or etched into

395 bedrock by carbonate dissolution<sup>61</sup>. Both types close through ice creep. When developing and  
396 reaching steady-state, a subglacial channel tends to have lower water pressure than cavities,  
397 which therefore drains the connected cavity system.

398

399

400

#### 401 **Acknowledgments**

402

403 This work has been conducted in the framework of the RESOLVE Project (<https://resolve.osug.fr/>)  
404 (LabEx OSUG@2020, Investissement d'avenir – ANR10LABX56 and IDEX Université Grenoble  
405 Alpes). Most of the computations presented in this paper were performed using the GRICAD  
406 infrastructure (<https://gricad.univ-grenoble-alpes.fr>), which is supported by Grenoble research  
407 communities, and with the CiGri tool (<https://github.com/oar-team/cigri>) that was developed by  
408 Gricad, Grid5000 (<https://www.grid5000.fr>) and LIG (<https://www.liglab.fr/>). FG acknowledges  
409 support from ANR SEISMORIV (ANR-17-CE01-0008) and SAUSSURE (ANR-18-CE01-0015-01).

410 We thank Christian Vincent and Nathan Maier for feedback on paper writing and data  
411 interpretation. We thank Agnès Helmstetter and Benoit Urruty for fruitful discussion on data  
412 analysis. We thank Mondher Chekki for numerical support dealing with the dense seismic array  
413 big dataset. U.N. thanks Aurélien Mordret, Amandine Sergeant, Léonard Seydoux, Jean  
414 Soubestre, and Josefine Umlauf for discussions on locating spatially spread seismic noise  
415 sources, and we thank Camillo Rada for discussions on subglacial drainage. U.N. thanks Pete  
416 Akers, Jordi Bolibar, Fanny Brun, David Laliche, Fabien Moustard, Hans Segura and Jonathan  
417 Wille for fruitful discussions on this work.

#### 418 **Codes and data availability**

419 The time series of physical quantities measured at Argentière glacier over the 2017 and 2018  
420 melt-season can be found at <https://doi.org/10.5281/zenodo.3701520>. All of the data associated  
421 with the dense array experiment can be found at <https://doi.org/10.5281/zenodo.3971815>. The  
422 spatial maps of source locations, glacier geometries and hydraulic potentials as well as the code  
423 used to processed these data can be found at <https://doi.org/10.5281/zenodo.4024660>. Part of  
424 the dataset of the seismic signals acquired during RESOLVE-Argentière can be found at  
425 [https://doi.org/10.15778/RESIF\\_ZO2018](https://doi.org/10.15778/RESIF_ZO2018) in link with ref.<sup>30</sup>. Contact U.N. at  
426 ugo.nanni0158@gmail.com or [ugo.nanni@univ-grenoble-alpes.fr](mailto:ugo.nanni@univ-grenoble-alpes.fr) for questions related to the  
427 above described datasets and codes.

428

429

#### 430 **References**

- 431 1. Shreve, R. L. Movement of Water in Glaciers. *J. Glaciol.* **11**, 205–214 (1972).
- 432 2. Iken, A. L. M. U. T., Truffer, M. & Truffe, M. The relationship between subglacial water  
433 pressure and velocity of Findelengletscher, Switzerland, during its advance and retreat. *J.*  
434 *Glaciol.* **43**, 328–338 (1997).
- 435 3. Davison, B. J., Sole, A. J., Livingstone, S. J., Cowton, T. R. & Nienow, P. W. The influence  
436 of hydrology on the dynamics of land-terminating sectors of the Greenland ice sheet.  
437 *Front. Earth Sci.* **7**, (2019).
- 438 4. Sole, A. J. *et al.* Seasonal speedup of a Greenland marine-terminating outlet glacier  
439 forced by surface melt-induced changes in subglacial hydrology. *J. Geophys. Res. Earth*  
440 *Surf.* **116**, 1–11 (2011).
- 441 5. Ritz, C. *et al.* Potential sea-level rise from Antarctic ice-sheet instability constrained by  
442 observations. *Nature* **528**, 115–118 (2015).
- 443 6. King, M. D. *et al.* Dynamic ice loss from the Greenland Ice Sheet driven by sustained

- 444 glacier retreat. *Commun. Earth Environ.* **1**, 1–7 (2020).
- 445 7. Lliboutry, L. General Theory of Subglacial Cavitation and Sliding of Temperate Glaciers. *J.*  
446 *Glaciol.* **7**, 21–58 (1968).
- 447 8. Röthlisberger, H. Water Pressure in Intra- and Subglacial Channels. *J. Glaciol.* **11**, 177–  
448 203 (1972).
- 449 9. Kamb, B. Glacier surge mechanism based on linked cavity configuration of the basal  
450 water conduit system. *J. Geophys. Res.* **92**, 9083 (1987).
- 451 10. Hubbard, B. P., Sharp, M. J., Willis, I., Nielsen, M. K. & Smart, C. C. Borehole water-level  
452 variations and the structure of the subglacial hydrological system of Haut Glacier d' Arolla  
453 ,. *J. Glaciol.* **41**, 572–583 (1995).
- 454 11. Schoof, C. Ice-sheet acceleration driven by melt supply variability. *Nature* **468**, 803–806  
455 (2010).
- 456 12. Tedstone, A. J. *et al.* Decadal slowdown of a land-terminating sector of the Greenland Ice  
457 Sheet despite warming. *Nature* **526**, 692–695 (2015).
- 458 13. Andrews, L. C. *et al.* Direct observations of evolving subglacial drainage beneath the  
459 Greenland Ice Sheet. *Nature* **514**, 80–83 (2014).
- 460 14. Rada, C. & Schoof, C. Channelized, distributed, and disconnected: Subglacial drainage  
461 under a valley glacier in the Yukon. *Cryosphere* **12**, 2609–2636 (2018).
- 462 15. Hoffman, M. J. *et al.* Greenland subglacial drainage evolution regulated by weakly  
463 connected regions of the bed. *Nat. Commun.* **7**, 13903 (2016).
- 464 16. Sole, A. *et al.* Winter motion mediates dynamic response of the Greenland Ice Sheet to  
465 warmer summers. *Geophys. Res. Lett.* **40**, 3940–3944 (2013).
- 466 17. Williams, J. J., Gourmelen, N. & Nienow, P. Dynamic response of the Greenland ice sheet

- 467 to recent cooling. *Sci. Rep.* **10**, 1–11 (2020).
- 468 18. Nienow, P., Sharp, M. & Willis, I. Seasonal changes in the morphology of the subglacial  
469 drainage system, Haut Glacier d’Arolla, Switzerland. *Earth Surf. Process. Landforms* **23**,  
470 825–843 (1998).
- 471 19. Tranter, M., Brown, G. H., Hodson, A. J. & Gurnell, A. M. Hydrochemistry as an indicator  
472 of subglacial drainage system structure: a comparison of Alpine and Sub-Polar  
473 environments. *Hydrol. Process.* **10**, 541–556 (1996).
- 474 20. Chandler, D. M. *et al.* Evolution of the subglacial drainage system beneath the Greenland  
475 Ice Sheet revealed by tracers. *Nat. Geosci.* **6**, 195–198 (2013).
- 476 21. Bartholomaus, T. C., Amundson, J. M., Walter, J. I., O’Neel, S., West, M. E. & Larsen, C.  
477 F. Subglacial discharge at tidewater glaciers revealed by seismic tremor. *Geophys. Res.*  
478 *Lett.* **42**, 6391–6398 (2015).
- 479 22. Gimbert, F. *et al.* Subseasonal changes observed in subglacial channel pressure, size,  
480 and sediment transport. *Geophys. Res. Lett.* **43**, 3786–3794 (2016).
- 481 23. Nanni, U. *et al.* Quantification of seasonal and diurnal dynamics of subglacial channels  
482 using seismic observations on an Alpine glacier. *Cryosphere* **14**, 1475–1496 (2020).
- 483 24. Vore, M. E., Bartholomaus, T. C., Winberry, J. P., Walter, J. I. & Amundson, J. M. Seismic  
484 Tremor Reveals Spatial Organization and Temporal Changes of Subglacial Water System.  
485 *J. Geophys. Res. Earth Surf.* **124**, 427–446 (2019).
- 486 25. Lindner, F., Walter, F., Laske, G. & Gimbert, F. Glaciohydraulic seismic tremors on an  
487 Alpine glacier. *Cryosphere* **14**, 287–308 (2020).
- 488 26. Burtin, A., Vergne, J., Rivera, L. & Dubernet, P. Location of river-induced seismic signal  
489 from noise correlation functions. *Geophys. J. Int.* **182**, 1161–1173 (2010).

- 490 27. Rost, S. & Thomas, C. Array seismology: Methods and applications. *Rev. Geophys.* **40**, 2-  
491 1-2-27 (2002).
- 492 28. Kuperman, W. A. & Turek, G. Matched field acoustics. *Mech. Syst. Signal Process.* **11**,  
493 141–148 (1997).
- 494 29. Almendros, J., Ibáñez, J. M., Alguacil, G. & Del Pezzo, E. Array analysis using circular-  
495 wave-front geometry: An application to locate the nearby seismo-volcanic source.  
496 *Geophys. J. Int.* **136**, 159–170 (1999).
- 497 30. Gimbert, F. *et al.* A Multi-Physics Experiment with a Temporary Dense Seismic Array on  
498 the Argentière Glacier, French Alps: The RESOLVE Project. *Seismol. Res. Lett.* (2021).  
499 doi:10.1785/0220200280
- 500 31. Vincent, C. & Moreau, L. Sliding velocity fluctuations and subglacial hydrology over the  
501 last two decades on Argentière glacier, Mont Blanc area. *J. Glaciol.* **62**, 805–815 (2016).
- 502 32. Sergeant, A. *et al.* On the Green's function emergence from interferometry of seismic  
503 wave fields generated in high-melt glaciers: Implications for passive imaging and  
504 monitoring. *Cryosphere* **14**, 1139–1171 (2020).
- 505 33. Legaz, A. *et al.* Self-potential and passive seismic monitoring of hydrothermal activity: A  
506 case study at Iodine Pool, Waimangu geothermal valley, New Zealand. *J. Volcanol.*  
507 *Geotherm. Res.* **179**, 11–18 (2009).
- 508 34. Chmiel, M., Roux, P. & Bardainne, T. High-sensitivity microseismic monitoring: Automatic  
509 detection and localization of subsurface noise sources using matched-field processing and  
510 dense patch arrays. *Geophysics* **84**, KS211–KS223 (2019).
- 511 35. Venkatesh, S. R., Polak, D. R. & Narayanan, S. Beamforming algorithm for distributed  
512 source localization and its application to jet noise. *AIAA J.* **41**, 1238–1246 (2003).

- 513 36. Gimbert, F. *et al.* Seismological Research Letters The RESOLVE project : a multi-physics  
514 experiment with a temporary dense seismic array on the Argentière Glacier , French Alps.  
515 *Seismol. Res. Lett.* (2020).
- 516 37. Sergeant, A. *et al.* On the Green ' s function emergence from interferometry of seismic  
517 wavefields generated in high-melt glaciers : implications for passive imaging and  
518 monitoring. 1–52 (2019).
- 519 38. Aki, K. & Richards, P. G. *Quantitative seismology.* (University Science Books,U.S., 2002).
- 520 39. Lliboutry, L. Modifications to the theory of intraglacial waterways for the case of subglacial  
521 ones. *J. Glaciol.* **29**, 216–226 (1983).
- 522 40. Kavanaugh, J. L. & Clarke, G. K. C. Abrupt glacier motion and reorganization of basal  
523 shear stress following the establishment of a connected drainage system. *J. Glaciol.* **47**,  
524 472–480 (2001).
- 525 41. Nienow, P. W., Sharp, M. & Willis, I. C. Velocity–discharge relationships derived from dye  
526 tracer experiments in glacial meltwaters: implications for subglacial flow conditions.  
527 *Hydrol. Process.* **10**, 1411–1426 (1996).
- 528 42. de Fleurian, B. *et al.* A modeling study of the effect of runoff variability on the effective  
529 pressure beneath Russell Glacier, West Greenland. *J. Geophys. Res. F Earth Surf.* **121**,  
530 1834–1848 (2016).
- 531 43. Gillet-Chaulet, F. *et al.* Assimilation of surface velocities acquired between 1996 and 2010  
532 to constrain the form of the basal friction law under Pine Island Glacier. *Geophys. Res.*  
533 *Lett.* **43**, 10,311–10,321 (2016).
- 534 44. Booth, A. D. *et al.* Distributed Acoustic Sensing (DAS) of Seismic Properties in a Borehole  
535 drilled on a Fast-Flowing Greenlandic Outlet Glacier. *Geophys. Res. Lett.* 0–3 (2020).  
536 doi:10.1002/ESSOAR.10502609.1

- 537 45. Soubestre, J. *et al.* Journal of Geophysical Research : Solid Earth Network-Based  
538 Detection and Classification of Seismovolcanic Tremors : Example From the Klyuchevskoy  
539 Volcanic Group in Kamchatka. (2018). doi:10.1002/2017JB014726
- 540 46. Moreau, L. *et al.* Sea Ice Thickness and Elastic Properties From the Analysis of  
541 Multimodal Guided Wave Propagation Measured With a Passive Seismic Array. *J.*  
542 *Geophys. Res. Ocean.* **125**, 1–17 (2020).
- 543 47. Irrazaval, I., Werder, M. A. & Huss, M. Determining the evolution of an alpine glacier  
544 drainage system by solving inverse problems. 1–14 (2021).
- 545 48. Walter, F. *et al.* Distributed acoustic sensing of microseismic sources and wave  
546 propagation in glaciated terrain. *Nat. Commun.* **11**, (2020).
- 547 49. Soubestre, J. *et al.* Depth Migration of Seismovolcanic Tremor Sources Below the  
548 Klyuchevskoy Volcanic Group (Kamchatka) Determined From a Network-Based Analysis.  
549 *Geophys. Res. Lett.* **46**, 8018–8030 (2019).
- 550 50. Mordret, A., Roux, P., Boué, P. & Ben-Zion, Y. Shallow three-dimensional structure of the  
551 San Jacinto fault zone revealed from ambient noise imaging with a dense seismic array.  
552 *Geophys. J. Int.* **216**, 896–905 (2019).
- 553 51. Bakker, M. *et al.* Field Application and Validation of a Seismic Bedload Transport Model.  
554 *J. Geophys. Res. Earth Surf.* **125**, 0–3 (2020).
- 555 52. Vincent, C., Soruco, A., Six, D., Le Meur, E. & Meur, E. L. E. Glacier thickening and decay  
556 analysis from 50 years of glaciological observations performed on Glacier d'Argentière,  
557 Mont Blanc area, France. *Ann. Glaciol.* **50**, 73–79 (2009).
- 558 53. Hantz, D. & Lliboutry, L. Waterways, ice permeability at depth, and water pressures at  
559 Glacier d'Argentiere, French Alps. *J. Glaciol.* **29**, 227–239 (1983).



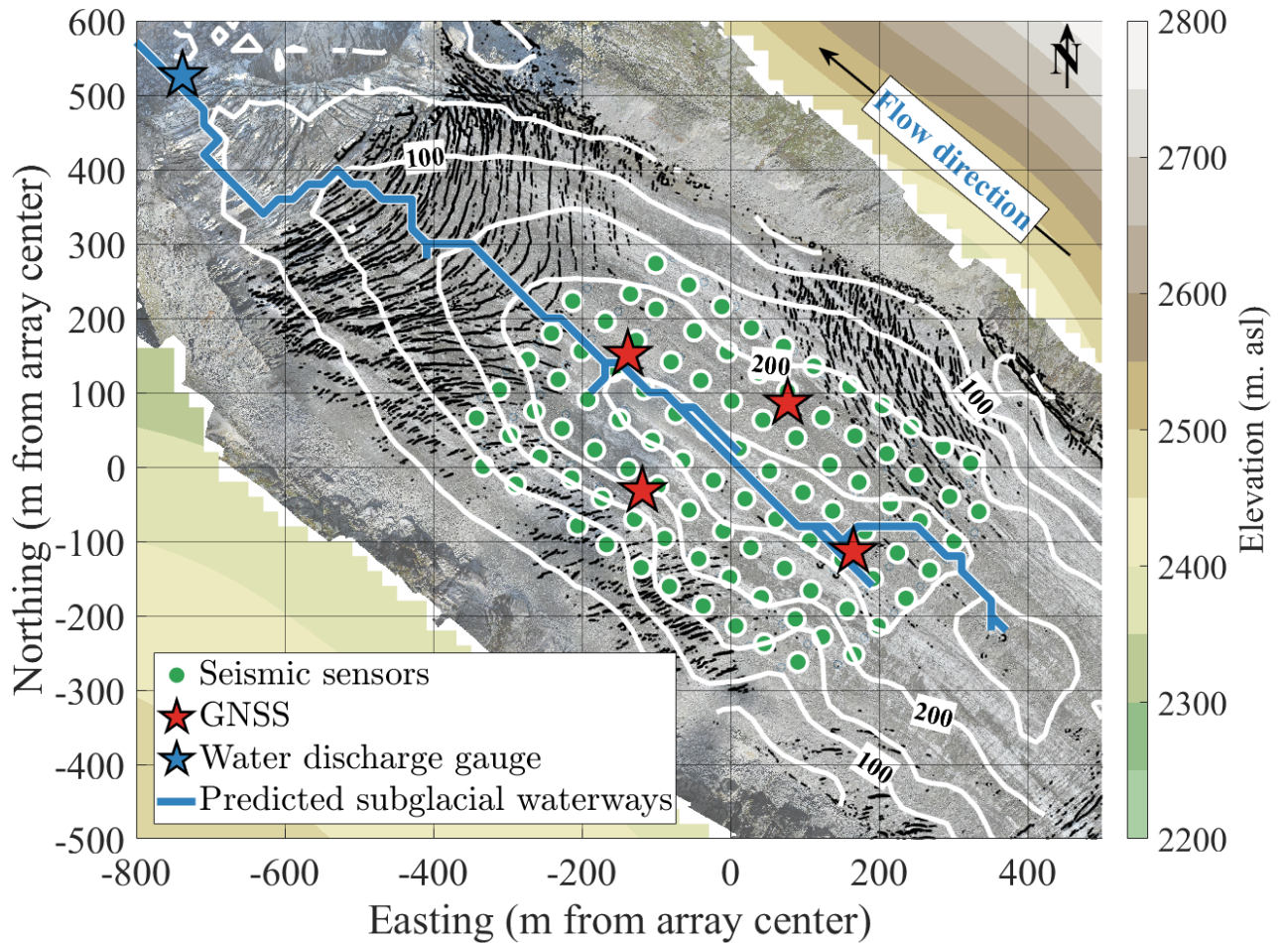
- 560 54. Nelder. Improved simplex method for function minimization. *Proceedings of the IEEE*  
561 *International Conference on Systems, Man and Cybernetics* **3**, 1702–1705 (1996).
- 562 55. Chmiel, M., Roux, P. & Bardainne, T. Extraction of phase and group velocities from  
563 ambient surface noise in a patch-array configuration. *Geophysics* **81**, KS231–KS240  
564 (2016).
- 565 56. Pyrak-nolte, L. J., Mullenbach, B. L., Li, X., Nolte, D. D. & Grader, A. S. synthetic  
566 sediments using seismic wave transmission Sample. *Geophys. Res. Lett.* **26**, 127–130  
567 (1999).
- 568 57. Willis, I., Lawson, W., Owens, I., Jacobel, B. & Autridge, J. Subglacial drainage system  
569 structure and morphology of Brewster Glacier, New Zealand. *Hydrol. Process. An Int. J.*  
570 **23**, 384–396 (2009).
- 571 58. Schwanghart, W. & Scherler, D. Short Communication: TopoToolbox 2 - MATLAB-based  
572 software for topographic analysis and modeling in Earth surface sciences. *Earth Surf.*  
573 *Dyn.* **2**, 1–7 (2014).
- 574 59. De Fleurian, B. *et al.* A double continuum hydrological model for glacier applications.  
575 *Cryosphere* **8**, 137–153 (2014).
- 576 60. Nye, J. F. The Flow of a Glacier in a Channel of Rectangular, Elliptic or Parabolic Cross-  
577 Section. *J. Glaciol.* **5**, 661–690 (1965).
- 578 61. Hallet, B. The Effect of Subglacial Chemical Processes on Glacier Sliding. *J. Glaciol.* **17**,  
579 209–221 (1976).
- 580
- 581

582

583 **Figures and Tables**

584

585 **Figure 1.**



586

587 Monitoring set-up of Glacier d'Argentière. Aerial view of the Glacier d'Argentière field site (France,

588 Mont Blanc mountain range) and location of the instruments used in this study. The seismic

589 network (green dots) is composed of 98 seismic stations with Fairfield Nodal Z-Land 3

590 components, which are indicated according to their positions at the beginning of the survey

591 period. Surface displacement was measured through four GNSS stations that functioned during

592 the study period (red stars). Subglacial water discharge (blue star) was measured through direct

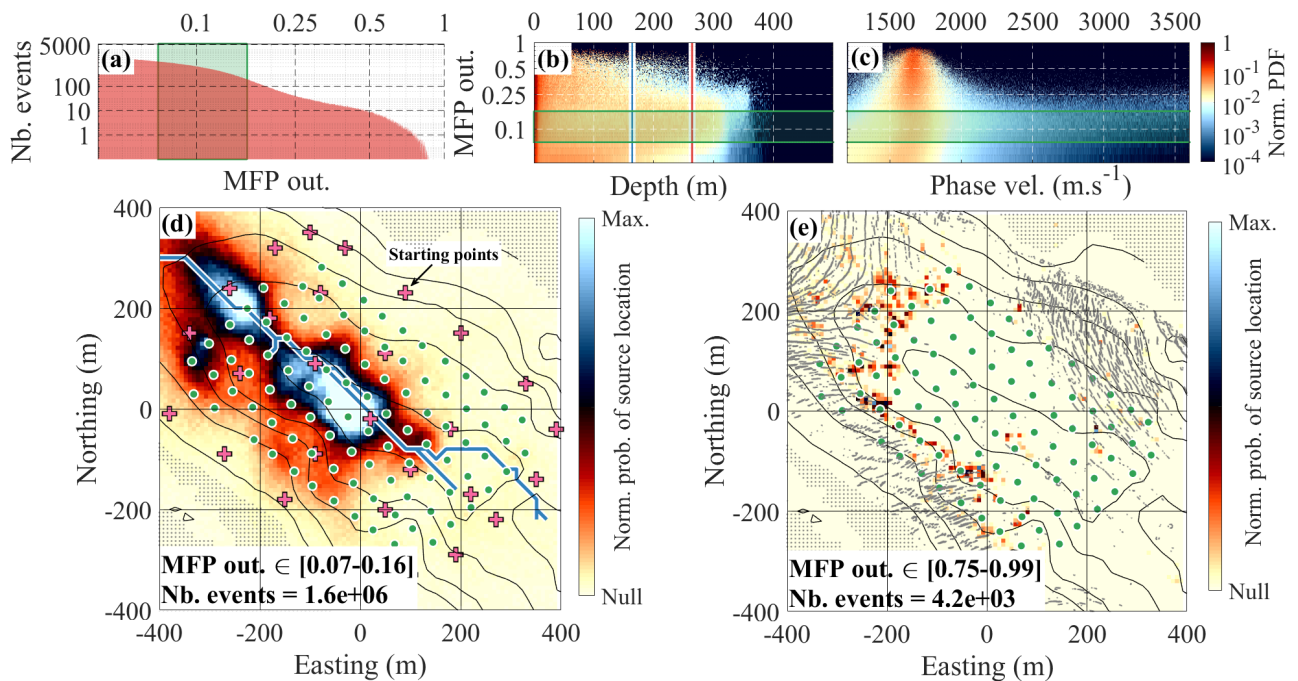
593 access to the glacier base from excavated tunnels. White contour lines show 50-m-spaced ice  
594 thickness contours, as obtained from combined radar measurements and surface elevations. The  
595 blue line shows the subglacial waterways as predicted from hydraulic potential calculations (see  
596 Methods). The glacier flows toward the northwest (top left). Aerial view provided by Bruno  
597 Jourdain.

598

599

600

601 **Figure 2.**



602

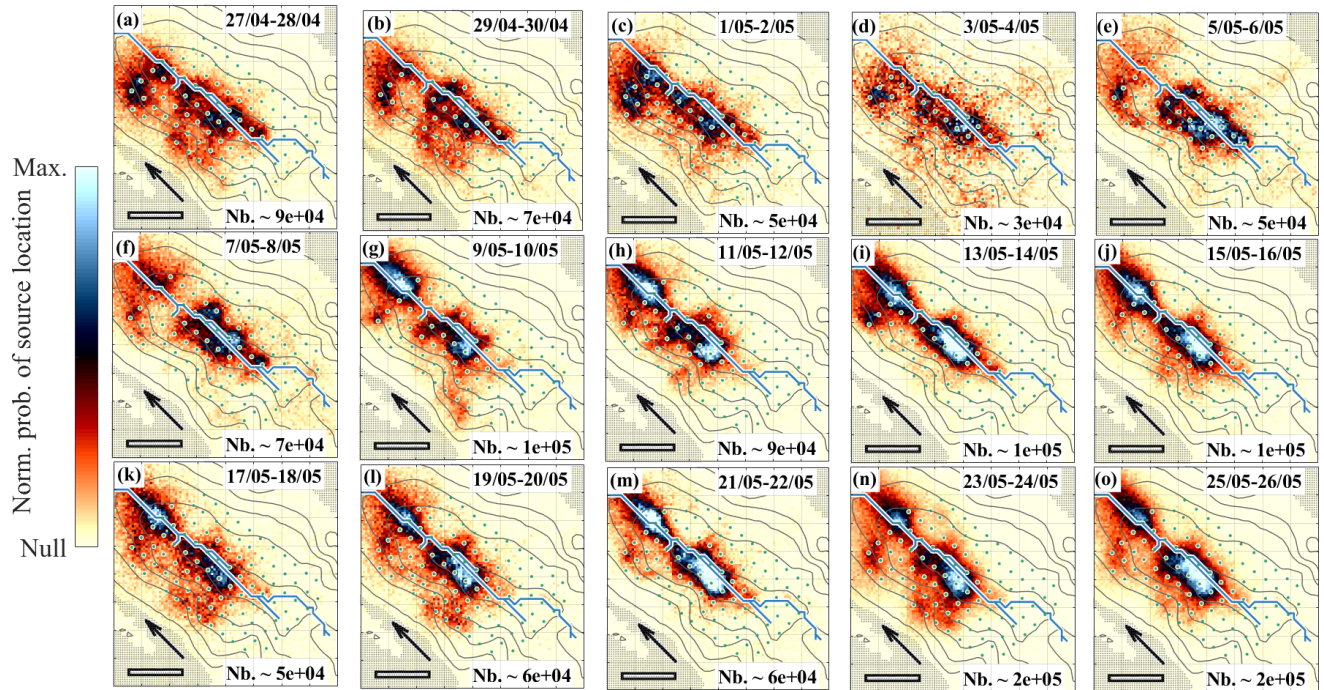
603 Statistics and two-dimensional representation of the matched-field processing (MFP) output for  
604 the  $5 \pm 2$  Hz frequency range. (a) Distribution of the average number of events located per day  
605 after applying the selection as a function of the MFP output. Green shaded area shows the [0.07-  
606 0.16] MFP output range for which the spatial distribution of the sources was investigated. (b)  
607 Normalized probability distribution of the MFP output as a function of source depth relative to the  
608 surface. The vertical red line shows the maximum ice thickness; the blue line shows the median  
609 ice thickness. The green shaded areas show the [0.07-0.16] MFP output range. (c) Normalized  
610 probability distribution of the MFP output as a function of the phase velocity. Note that the color  
611 scales are logarithmic and the distribution is normalized per MFP output band of 0.01. The green  
612 shaded areas show the [0.07-0.16] MFP output range. (d, e) Two-dimensional representation of  
613 the normalized probability of the source location obtained with  $8 \times 8$  m<sup>2</sup> pixels grid for the study  
614 area for the two MFP output ranges [0.07-0.16] (d) and [0.75-0.99] (e). Contour lines show 50-m-

615 spaced ice thickness contours, as shown in Figure 1. The gray shading shows ice-free areas. The  
616 green dots show the seismic array. The blue line in (d) shows the subglacial waterways as  
617 predicted from the hydraulic potential calculation, as shown in Figure 1. The black dots in (e)  
618 show crevasse locations, as shown in Figure 1. The pink crosses in (d) show the locations of the  
619 29 starting points used in the location algorithm.

620

621 **Figure 3.**

622



623

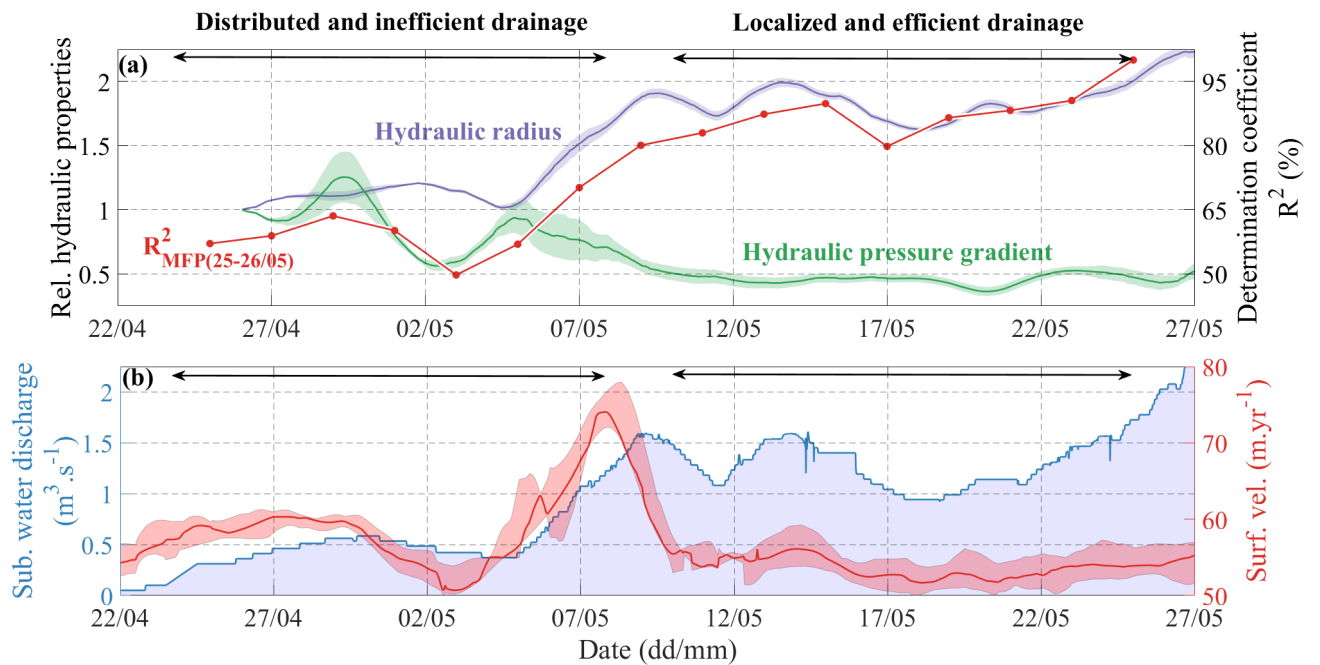
624 Two-dimensional maps of subglacial water flow source location obtained from matched-field  
625 processing (MFP). Temporal evolution of the spatial patterns of the source location densities  
626 obtained for the  $5 \pm 2$  Hz frequency range and the [0.07-0.16] MFP output range. All of the maps  
627 are averaged over 2-day time windows, with the associated number of the sources located shown  
628 in the bottom right corner (Nb.). Color scale ranges are normalized for each time window using  
629 maximum probability. (o) The characteristic pattern used in Figure 4 for calculation of the  
630 coefficient of determination. Contour lines show the 50-m-spaced ice thickness contours, as  
631 shown in Figure 1. The gray shading shows ice-free areas. Scale bars (bottom left): 200 m. The  
632 blue lines show the subglacial waterways, as predicted from the hydraulic potential calculation,  
633 and as shown in Figure 1. Black arrows show glacier and subglacial water flow directions.

634



636 **Figure 4.**

637



638

639 Temporal evolution of the subglacial hydraulic properties, seismic observations, and glacier flow.

640 (a) Left axis shows the relative hydraulic properties, as averaged over the 98 sensors. Hydraulic  
641 pressure gradient with  $\pm 1$  median absolute deviation (MAD), as the shaded envelope (green), and

642 hydraulic radius with  $\pm 1$  MAD, as the shaded envelope (purple). Both values are expressed as

643 relative to April 26. Right axis shows temporal evolution of the spatialized seismic observations

644 using the determination coefficient  $R^2$  of the source location pattern shown in Figure 3o (red).

645 The closer this coefficient is to 1, the more the drainage system is observed to be channelized.

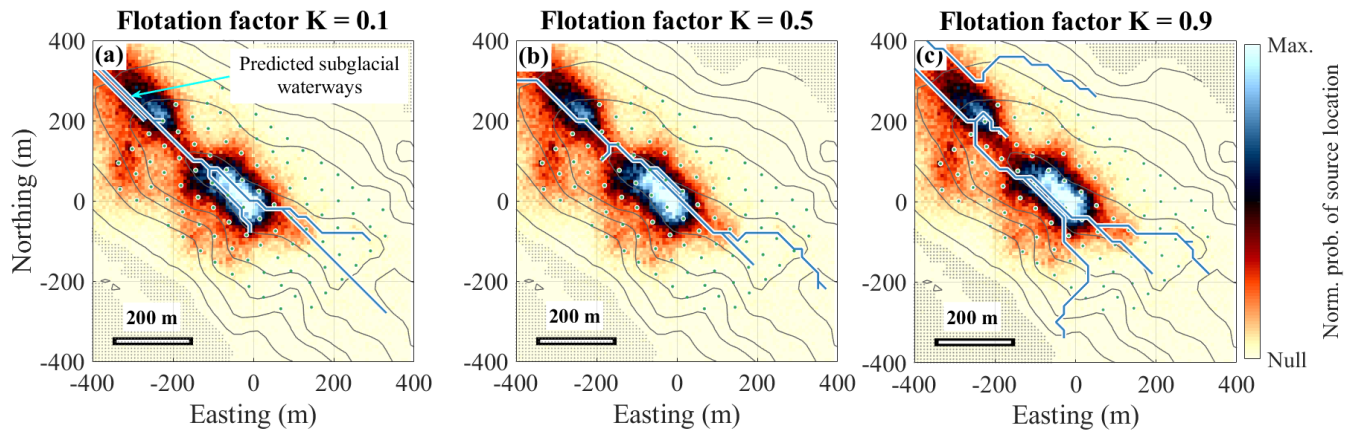
646 (b) Subglacial water discharge (blue line) with shaded blue area under the curve added for ease

647 of reading. Median surface velocity over the four on-ice GNSS stations (red line) with the

648 minimum/maximum shaded envelope.

649 **Supplementary Figure 1.**





650

651 Two-dimensional representation of the normalized probability of the source location obtained with  
 652  $8 \times 8$  m<sup>2</sup> pixels grid for the study area for the two MFP output ranges [0.07-0.16] as shown in Fig.  
 653 2d. The blue line shows the subglacial waterways as predicted from hydraulic potential  
 654 calculations for three different values of flotation fraction K (see Methods for details). Green dots  
 655 show seismic sensors location.